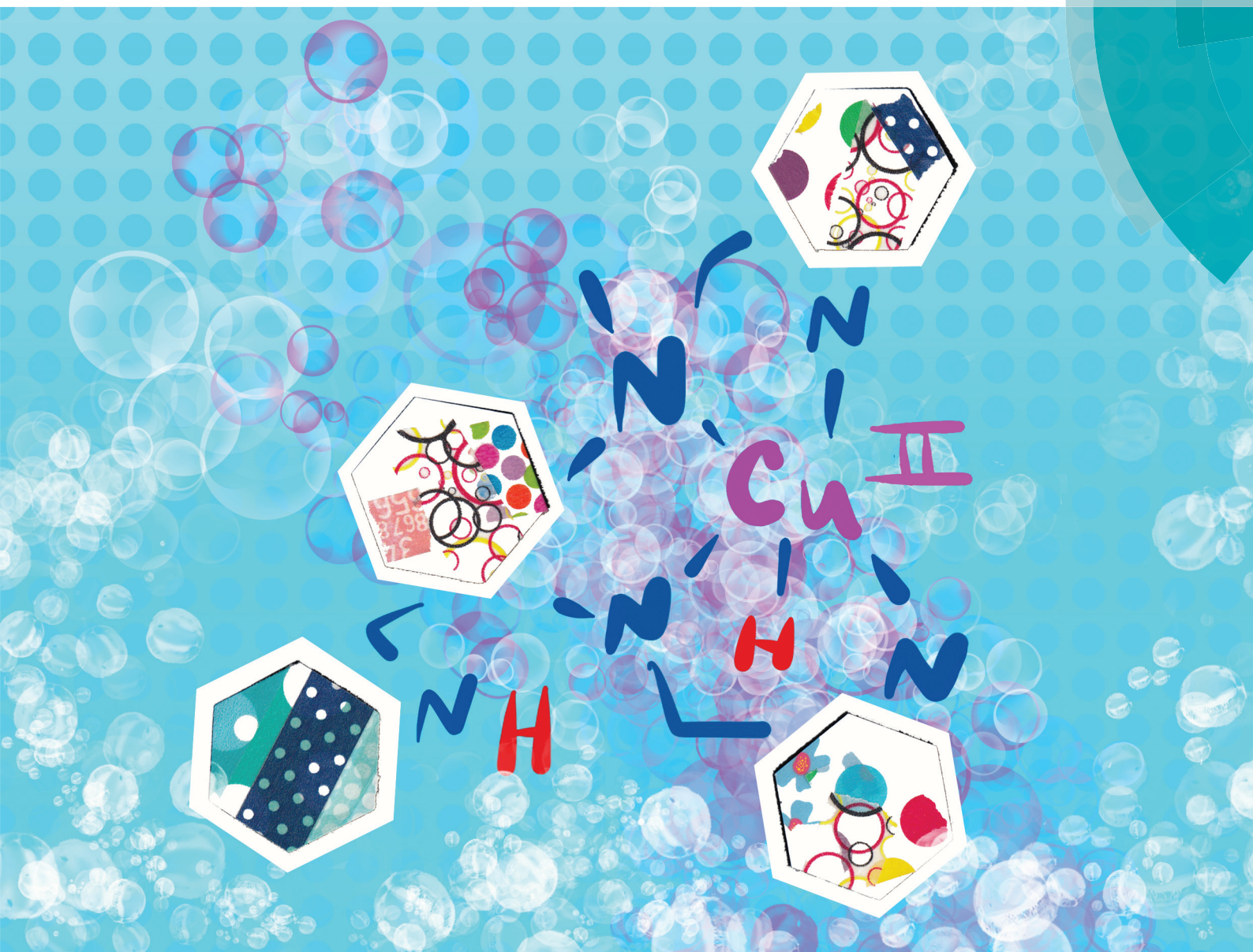


Dalton Transactions

An international journal of inorganic chemistry

rsc.li/dalton



ISSN 1477-9226





PAPER

Shivnath Mazumder, Cláudio N. Verani *et al.*

A pentadentate nitrogen-rich copper electrocatalyst for water reduction with pH-dependent molecular mechanisms

Cite this: *Dalton Trans.*, 2017, **46**, 16812

A pentadentate nitrogen-rich copper electrocatalyst for water reduction with pH-dependent molecular mechanisms†

Danushka M. Ekanayake,^a Krista M. Kulesa,^a Jaffarguriqbal Singh,^b Kenneth K. Kpogo,^a Shivnath Mazumder,^{*b} H. Bernhard Schlegel ^a and Cláudio N. Verani ^{*a}

The new pentadentate 3d⁹ complex [Cu^{II}(L^{N2Py3})](PF₆)₂ (**1**) based on a nitrogen-rich framework acts as an electrocatalyst toward dihydrogen production from water. This species is active at pHs 7 and 2.5 yielding respective TON_{3h} values of 1670 and 3900. Comparison of the molecular structure of **1** with that of the reduced [Cu^I(L^{N2Py3})]PF₆ (**2**) evidences elongated Cu–N bond lengths resulting from an increased electron density around the 3d¹⁰ Cu^I center. The absence of nanoparticulate formation indicates that molecular mechanisms prevail at both pHs. Furthermore, experimental and DFT data support that distinct mechanisms are operative: while the metal center plays a key role at pH 7, one dangling pyridine moiety gets protonated at pH 2.5 and becomes actively involved in a relay mechanism. In both cases the Cu^{III}–H[–] intermediate seems to be bypassed by PCET processes.

Received 25th July 2017,
Accepted 30th August 2017

DOI: 10.1039/c7dt02711g

rsc.li/dalton

Introduction

Molecular catalysts for water reduction that incorporate earth-abundant transition metals have gained especial attention in facilitating electrocatalytic H₂ production. A number of transition metal complexes containing cobalt,^{1,2} nickel,^{3,4} and less often, iron^{5,6} have been considered as capable of stabilizing reactive hydrides required for dihydrogen generation.

Copper has gained particular interest due to its abundance and price, but considerable hurdles must be overcome before this metal becomes a mainstream option for catalyst design. Unlike the cobalt ion that displays energetically affordable conversions from 3d⁶ Co^{III} to 3d⁷ Co^{II} to 3d⁸ Co^I species,^{7–10} formation of the 3d⁸ Cu^{III} from the abundant 3d⁹ Cu^{II} species requires high potentials that may lead to ligand-based radical species^{11–14} in absence of proton-coupled electron transfer mechanisms. Additionally, the monovalent Cu^I species is labile due to the zero ligand field stabilization energy associ-

ated with its 3d¹⁰ configuration. This lability is associated with the deposition of metallic Cu⁰ and Cu₂O crystallites recently observed by Siewert *et al.*¹⁵ for imidazole/pyridine ligands and ascribed as the active catalysts.

Recent examples of proton and water reduction events attributed to molecular catalysts involve triazenido, oxamido and hydroxybenzylideneimino species by Zhan *et al.*^{16,17} and pentadentate pyridine-based ligand systems by Wang *et al.*¹⁸ The former operate at a neutral pH and require relatively high overpotentials; the later lead to copious hydrogen generation in acidic media (pH 2.5).

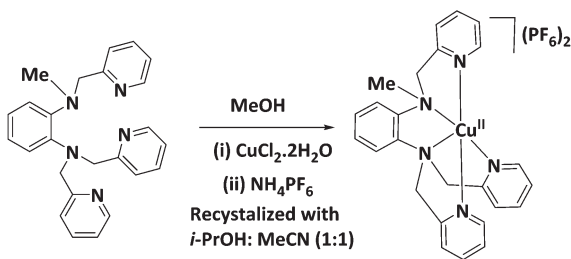
Considering these results, we hypothesize that the design of robust Cu-based catalysts must include polydentate chelates capable of providing donor groups that minimize the intrinsic lability of the Cu^I ion. As such, based on the behavior of our own cobalt analog,¹⁰ we synthesized the pentadentate pyridine-rich Cu^{II} system [Cu^{II}(L^{N2Py3})](PF₆)₂ (**1**) shown in Scheme 1 and investigated its catalytic activity towards water reduction.

Species **1** will be catalytically active towards water reduction either by (i) reduction of Cu^{II} to Cu^I followed by a PCET step to yield a [Cu^{II}–H[–]], or by (ii) formation of a ligand radical *via* [Cu^{II}L] → [Cu^IL] → [Cu^IL[•]], which then forms a Cu^{II}–H[–] species. Furthermore, the 3d⁹ to 3d¹⁰ reduction will lead to geometric changes that foster detachment of some pyridine arms. In acidic media these moieties are likely to become protonated and lead to distinct pH-dependent mechanisms. The results follow.

^aDepartment of Chemistry, Wayne State University, 5101 Cass Ave, Detroit, MI 48202, USA. E-mail: cnverani@chem.wayne.edu

^bDepartment of Chemistry, Hofstra University, Berliner Hall, Hempstead, NY 11549, USA. E-mail: shivnath.mazumder@hofstra.edu

† Electronic supplementary information (ESI) available: Crystallographic parameters, UV-visible spectra, SEM and EDX analysis images, along with DFT calculations. CCDC 1563852 and 1563853. For ESI and crystallographic data in CIF or other electronic format see DOI: 10.1039/c7dt02711g



Scheme 1 Synthetic route for the $[\text{Cu}^{\text{II}}(\text{L}^{\text{N2Py3}})](\text{PF}_6)_2$ (**1**).

Results and discussion

Synthesis and characterization of (1) and (2)

The pentadentate ligand L^{N2Py3} was synthesized and characterized according to reported procedures.¹⁰ The divalent complex $[\text{Cu}^{\text{II}}(\text{L}^{\text{N2Py3}})](\text{PF}_6)_2$ (**1**) was obtained by treatment of the purified tripodal ligand with $\text{CuCl}_2 \cdot 2\text{H}_2\text{O}$ in MeOH under aerobic conditions for 2 h followed by counterion exchange with ammonium hexafluorophosphate. The monovalent complex $[\text{Cu}^{\text{I}}(\text{L}^{\text{N2Py3}})]\text{PF}_6$ (**2**) was synthesized under inert conditions using $[\text{Cu}(\text{CH}_3\text{CN})_4]\text{PF}_6$ in dry acetonitrile (MeCN). Both species were thoroughly characterized by multiple spectroscopic and spectrometric methods.

Molecular structures

X-ray quality crystals were obtained for blue colored **1** by slow evaporation from a 1 : 1 *i*-PrOH : MeCN mixture. The molecular structure of **1** is shown in Fig. 1a (also Tables T1–T3†) and consists of a discrete pentacoordinate $3d^9$ Cu^{II} ion bound to the $[\text{N}_2\text{N}'_3]$ donor set of the L^{N2Py3} ligand in a distorted square pyramidal environment¹⁹ with an associated τ value of 0.2. The amine N1 and N4 and the pyridine N2 and N5 nitrogen atoms compose the square basal plane, with the pyridine N3 occupying the apical position at a mean angle of 97.8° perpendicular to the plane. The $\text{Cu}-\text{N}_{\text{py}}$ bond distances 1.993(4) to 2.025(4) Å fall within reported range,^{18,20,21} while the apical pyridine is

slightly longer at 2.197(4) Å. Two PF_6^- counterions complete the structure of **1**.

The monovalent **2** was recrystallized in a 1 : 1 mixture of diethyl ether : MeCN yielding orange colored crystals. Two independent but very similar molecules are present in the asymmetric unit, and one of them is shown in Fig. 1b for simplicity. Like for the Cu^{II} species **1**, the ligand arrangement around **2** is distorted pentadentate around the $3d^{10}$ Cu^{I} ion with a τ value of 0.4. In spite of this similarity, considerable differences in bond lengths and angles are observed.

The amine N1, N4 and the pyridine N3 and N5 atoms form a square base, while the pyridine N2 atom occupies the apical position. The angle of the apical ligand is 101.3° perpendicular to the base. This increase in the mean angle reflects a distorted environment typical of a $3d^{10}$ geometry with an increased electron density around the copper center^{22–24} Similarly, the $\text{Cu}-\text{N}_{\text{py}}$ bond distances of **2** are slightly longer than those of **1**, with the exception of $\text{Cu}-\text{N}_3$, which is shorter by 0.21 Å. However, the $\text{Cu}-\text{N}_{\text{amine}}$ bonds in the monovalent **2** were significantly elongated, with the $\text{Cu}-\text{N}_1$ and $\text{Cu}-\text{N}_4$ being respectively longer by 0.38 Å and 0.32 Å than in **1**. This difference is attributed to the larger size of the monovalent copper center.

Redox and electronic behavior

The redox behavior of **1** was evaluated by cyclic voltammetry (CV) in MeCN using ferrocene as internal standard²⁵ (Fig. S1a†). The full-window CV profile from 0 to 2500 mV Fc/Fc^+ shows a quasi-reversible wave at $E_{1/2} = -460$ mV Fc/Fc^+ (-66 mV Ag/AgCl), assigned to the $\text{Cu}^{\text{II}}/\text{Cu}^{\text{I}}$ couple and directly relevant for catalysis.¹⁸ Other processes appear at -2200 mV Fc/Fc^+ (-1806 mV Ag/AgCl), attributed to ligand reduction $[\text{Cu}^{\text{I}}\text{L}]$, as well as a spike observed at -680 mV Fc/Fc^+ (-286 mV Ag/AgCl) and commonly attributed to $\text{Cu}^{\text{I}}/\text{Cu}^0$ reduction resulting from ligand reduction (Fig. S1b†). No peaks were observed on the anodic side of the voltammogram. The electronic spectrum of **1** in MeCN (Fig. S2†) showed a prominent UV band at 258 nm ($\epsilon = 16\,500$ $\text{M}^{-1} \text{cm}^{-1}$) assigned to an ligand-centered $\pi-\pi^*$ absorption along with a weak and broad visible absorption at 650 nm ($\epsilon = 150$ $\text{M}^{-1} \text{cm}^{-1}$) attributed to d–d processes of the $3d^9$ $\text{Cu}(\text{II})$ center.^{26,27} Due to interest in catalytic water reduction, the pale yellow one-electron reduced species obtained from **1** was also assessed *via* UV-visible spectroscopy after applying a sufficient potential (Fig. S3†). The resulting spectrum reveals a diminished $\pi-\pi^*$ band slightly hypsochromically shifted. A new band near 335 nm is assigned to a metal-to-ligand charge transfer band (MLCT),^{28–30} while the weak absorption at 650 nm disappears, as expected for a $3d^{10}$ configuration. Species **1** and its reduced counterpart were also investigated by EPR spectroscopy in MeCN at 110 K (Fig. 2). The spectrum associated with **1** is characteristic of an $S = 1/2$ signal with rhombic g-tensors at 2.020, 2.083, and 2.270 and collinear rhombic A-tensor for $\text{Cu}(\text{II})$ at 41, 67, and 400 MHz. The result corresponds to that of a $3d^9$ Cu^{II} complex in a distorted square pyramidal environment and with an unpaired electron occupying the $d_{x^2-y^2}$ molecular orbital with predomi-

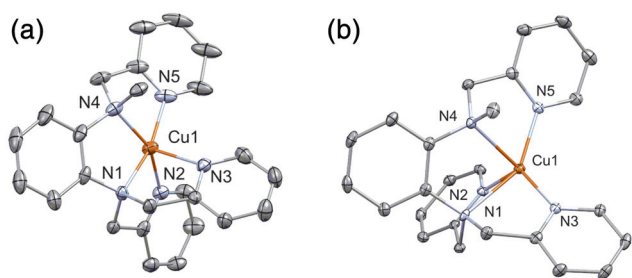


Fig. 1 ORTEP representations of (a) $[\text{Cu}^{\text{II}}(\text{L}^{\text{N2Py3}})]^{2+}$ (**1**; CCDC 1563852†), and (b) $[\text{Cu}^{\text{I}}(\text{L}^{\text{N2Py3}})]^+$ (**2**; CCDC 1563853†) at 50% probability. Selected bond lengths for **1**: $\text{Cu1}-\text{N1} = 2.025(4)$; $\text{Cu1}-\text{N2} = 1.993(4)$; $\text{Cu1}-\text{N3} = 2.197(4)$; $\text{Cu1}-\text{N4} = 2.013(4)$; $\text{Cu1}-\text{N5} = 2.001(4)$ Å. Selected bond lengths for **2**: $\text{Cu1}-\text{N1} = 2.415(2)$; $\text{Cu1}-\text{N2} = 2.066(2)$; $\text{Cu1}-\text{N3} = 1.998(2)$; $\text{Cu1}-\text{N4} = 2.332(2)$; $\text{Cu1}-\text{N5} = 2.039(2)$ Å. Hydrogen atoms omitted for clarity.

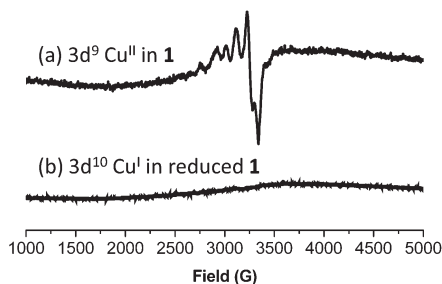


Fig. 2 EPR spectra of **1** before and after bulk electrolysis measured at 110 K in MeCN.

nant metal character. This result is approximate as the spectrum may indicate the presence of aggregates or slightly different structures, as discussed later in this paper. The spectrum of the $1e^-$ reduced **1** is typical of a silent $3d^{10} Cu^I$ ion similar to that found in **2**, and indicates that reduction of the metal center precedes ligand reduction.

Electrocatalytic water reduction

The catalytic ability of complex **1** towards water reduction was examined at two different pH values, namely, pH 2.5 and 7 using a three-electrode setup, with mercury pool as the working electrode.¹⁰ We start the discussion with pH 7. In presence of **1**, a catalytic peak appears at $-1490 mV_{Ag/AgCl}$. In order to obtain a more accurate value for the overpotential, a BE experiment was performed varying overpotentials from 183 mV to 1183 mV (Fig. S4†). Charge consumption was measured at intervals of 3 min (180 s), showing no charge consumption below 780 mV. At pH 7 in aqueous solution, the thermodynamic potential for H^+/H_2 is $-617 mV_{Ag/AgCl}$.³¹ This value is taken as the overpotential for hydrogen generation (Fig. 3). Electrocatalytic generation of hydrogen was attained from neutral water (pH = 7 phosphate buffer) with a catalyst concentration of $6 \mu mol L^{-1}$ at an applied potential of $-1700 mV_{Ag/AgCl}$. The total charge consumption in presence of the complex is approximately ninefold greater than that of the

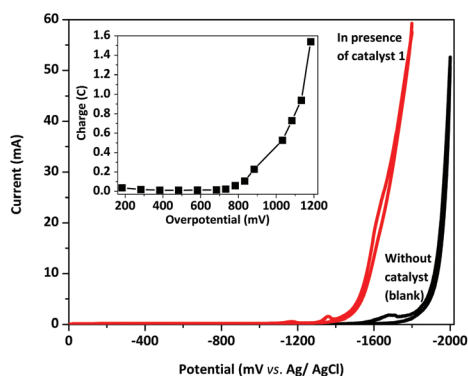


Fig. 3 Catalytic water reduction CV: Hg-pool; Ag/AgCl; Pt wire; 1 M phosphate buffer (pH 7); $100 mV s^{-1}$, inset: Precise determination of the overpotential for catalysis.

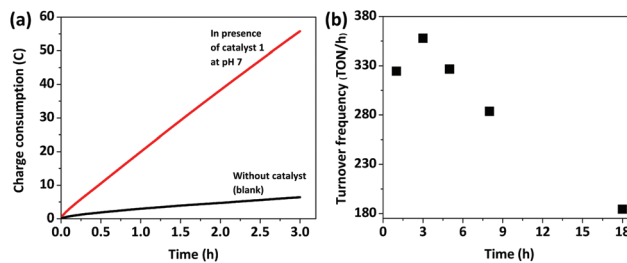


Fig. 4 (a) Charge vs. time plot for electrocatalytic hydrogen generation; $Q_{blank} = 6 C$ and $Q_{complex} = 56 C$ (b) dependence of the catalytic activity over time (CV/BE): Hg-pool; Ag/AgCl; Pt wire/coil; phosphate buffer (pH: 7); AP: $-1700 mV_{Ag/AgCl}$ (BE). Concentration of the complex = $6 \mu mol L^{-1}$.

blank solution (Fig. 4a). The linear behavior of the Q vs. t plot attests to the resilience of the catalyst over the duration of the experiment. A TON of 1670 was calculated after 3 h with an associated Faradaic efficiency of *ca.* 90%.

This result is comparable to the TON_{3h} observed for the structurally related cobalt catalyst¹⁰ (1615), and better than the equivalent nickel catalyst³² at 1050. This comparison is significant because these systems were analyzed using similar pH values, applied potentials and methodologies.

Catalysis performed for 18 h yielded a subsequent 3060 TON with a Faradaic efficiency of 45% suggestive of decreased activity likely related to catalyst deactivation over time. To understand the catalytic dependence with time, electrolysis was performed continuously for 18 h while periodically measuring the concentration of H_2 .

The resulting TOFs were calculated and are presented in Fig. 4b. The highest TOF was obtained after 3 h with a gradual decrease thereafter. These results corroborate with the idea of a vigorous initial molecule-based mechanism of dihydrogen generation that leads to eventual catalyst deactivation.

These catalytic mechanisms in water were analyzed using DFT methods^{33,34} and the results are shown in Fig. 5. The five-coordinate complex **1** containing a $3d^9 Cu^{II}$ ion has a doublet ground spin state associated with a semifilled $d_{x^2-y^2}$ metal-based molecular orbital in good agreement with the EPR data. This species can undergo a one-electron reduction at a calculated potential of $-190 mV_{Fc/Fc+}$ to yield the five-coordinate $3d^{10} Cu^I$ complex **A**. The DFT-calculated redox potential is within the acceptable error in the range of 200 to 300 mV.³⁵ The latter complex has a singlet ground spin state. The Cu-(N) amine bond distances are fairly long at 2.46 Å and 2.50 Å, in **A**, in excellent agreement with the experimental X-ray structure. Addition of a proton to species **A** could form a Cu^{III} -hydride complex $[Cu^{III}-H^-]$ **B** but this event is unfavorable by at least $45 kcal mol^{-1}$. This observation reinforces the notion that a +3 oxidation state is unlikely for the Cu ion. Complex **A** can be further reduced by one electron to yield species **C** at $-2150 mV_{Fc/Fc+}$. This reduction event involves ligand reduction on the pyridine moieties giving rise to the $[Cu^I L^-]$ complex **C**. This idea is supported by the experimental evidence in which the current enhancement of the catalytic peak associated with

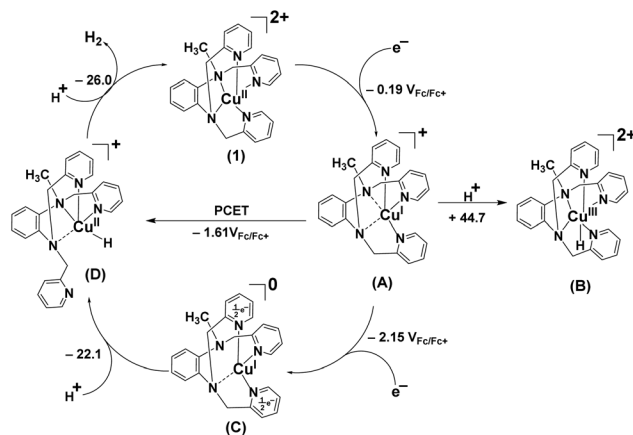


Fig. 5 Catalytic mechanism of H_2 generation by **1** in water at pH 7. It involves a proton-coupled electron transfer pathway from **A** to generate the $\text{Cu}^{\text{II}}\text{-H}^-$ species **D**. Free energies are in kcal mol^{-1} .

ligand reduction in the CV in presence of up to 10 acid equivalents (Fig. S5†). It is noteworthy that the radical is delocalized over two vicinal pyridine rings, and it was not possible to localize these charges on a single ring even after significant effort. The latter species is four-coordinate and adopts a distorted tetrahedral structure with one long Cu–N(amine) bond, 2.68 Å. Complex **C** has a doublet ground spin state. Addition of a proton to the metal center in **C** leads to the oxidation of the pyridine moieties to form the $\text{Cu}^{\text{II}}\text{-H}^-$ species **D**. The Cu^I center in **C** donates only one electron to the upcoming proton while the second electron is donated by the pyridine moieties. As a result, the protonation of **C** leading to the $\text{Cu}^{\text{II}}\text{-H}^-$ species **D** is favorable by about 22 kcal mol^{-1} , while the formation of a more demanding $\text{Cu}^{\text{III}}\text{-H}^-$ complex is avoided. Alternatively, a proton-coupled electron transfer (PCET) pathway from **A** to **D** that bypasses the pyridine-reduced complex **C** was also considered. The reduction potential of the PCET pathway has been calculated at $-1610 \text{ mV}_{\text{Fc}/\text{Fc}^+}$, thus in reasonable agreement with the experimentally measured onset potential $-1900 \text{ mV}_{\text{Fc}/\text{Fc}^+}$ observed for complex **1** at pH 7. Species **D** has been modelled with a five-coordinate Cu^{II} center where four N atoms are complemented by a proton and one uncoordinated or dangling pyridine. The species has a doublet ground spin state associated again with a semifilled $d_{x^2-y^2}$ MO. Addition of a second proton to species **D** releases dihydrogen and regenerates **1** enabling its re-entrance to the catalytic cycle. This event is energetically favorable by 26 kcal mol^{-1} .

The mechanisms of copper-containing **1** show considerable distinctions when compared to its congener catalysts containing Co^{II} and Ni^{II} bound to the $\text{L}^{\text{N}_2\text{Py}_3}$ ligand: the Co species¹⁰ favors formation of a metal-based $3d^6 \text{Co}^{\text{III}}\text{-H}^-$ at affordable potentials, whereas a $3d^7 \text{Ni}^{\text{III}}$ species³² is avoided by means of ligand involvement. Because a $3d^8 \text{Cu}^{\text{III}}\text{-H}^-$ species is energetically costly, and because the formation of radical species will lead to deactivation, molecular catalysis with **1** will likely involve PCET. For catalytic processes over 3 hours, this PCET step may give way to $\text{A} \rightarrow \text{C} \rightarrow \text{D}$ mechanisms responsible for

catalyst deactivation. There is no substantial evidence, experimental or otherwise, that protonation of the dangling pyridine takes place at pH 7.

Post-catalytic analysis of **1** at pH 7

Comparative UV-Visible spectra before and after 3 h catalysis (Fig. S6†) show the disappearance of a 260 nm peak associated with intraligand charge transfer, thus implying that transformation of the molecular catalyst takes place during the electrocatalytic process. Additional experiments were carried out to assess the nature of the copper catalyst, and a bulk electrolysis experiment was performed using a grafoil electrode as the working electrode to investigate the possibility of conversion of molecular **1** into nanocrystalline Cu_2O prior to catalysis.¹⁵

Two independent catalytic experiments were performed at 3 and 8 h; the post-catalysis grafoil electrode was rinsed with copious amounts of deionised water and compared against a control (blank) using scanning electron microscopy (SEM) to obtain images associated with different regions of the surface. These SEM images (Fig. S7†) indicate absence of nanocrystalline Cu_2O after 3 h, and only scant presence of nanoparticles after 8 h. Subsequent energy-dispersive X-ray spectroscopic (EDX) analysis of the grafoil surface (Fig. S8†) confirms the absence of Cu nanoparticles. Therefore, to the best of our knowledge, the experimentally observed lack of nanoparticulate materials suggests a molecule-based catalytic process. Although the mechanisms of deactivation remain elusive, it is evident that the molecular catalyst gets degraded. This process may explain the decrease in prolonged catalytic activity for **1** and is likely linked to changes in geometrical preferences associated with the $\text{Cu}^{\text{II}}/\text{Cu}^{\text{I}}$ redox couple.^{22–24}

Electrocatalytic dependence on pH and applied potential

The catalytic behavior of **1** was studied at pHs 7 and 2.5, as described, as well as with distinct applied potentials of -1400 and $-1700 \text{ mV}_{\text{Ag}/\text{AgCl}}$ for each case. The charge consumption at pH 7 and $-1700 \text{ mV}_{\text{Ag}/\text{AgCl}}$ is shown in Fig. 4a and has been discussed. As expected, no significant catalytic behavior is observed at that pH when the potential is lowered to $-1400 \text{ mV}_{\text{Ag}/\text{AgCl}}$, thus below the onset potential. However, at pH 2.5 considerable changes take place. Species **1** was tested for stability in phosphate buffer and yielded identical UV-Visible spectra over a period of 8 h (Fig. S9 and S10†), thus reinforcing the notion of a stable species at this pH. An applied potential of $-1400 \text{ mV}_{\text{Ag}/\text{AgCl}}$ leads to a distinct profile in which the charge *vs.* time curve shows an inflection starting after around 20 min of the catalysis and yielding considerably higher charge consumption (Fig. 6). When this experiment was performed over 3 h a quasi-sigmoidal *Q vs. t* curve was observed, in which the first inflection is followed by a plateau (Fig. S11†).

These profiles indicate that distinctive mechanisms of dihydrogen production are taking place. At first we suspected that the molecular catalyst had been converted into a different active form, possibly nanocrystalline Cu_2O .¹⁵ However, the comparative UV-Visible spectra from before and after catalysis

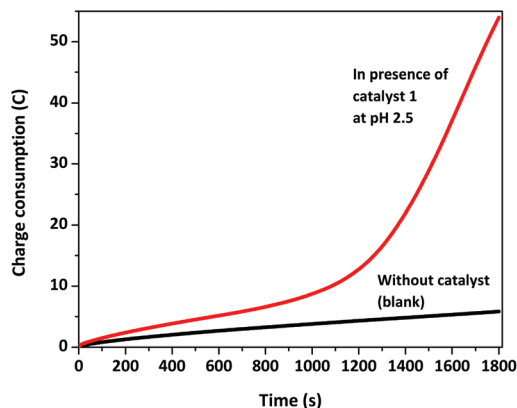


Fig. 6 Charge vs. time plot for **1** at an applied potential of $-1400\text{ mV}_{\text{Ag}/\text{AgCl}}$ at pH 2.5. Note the inflection after ca. 20 min suggestive of a relay mechanism involving protonation of a dangling pyridine arm.

(Fig. S12[†]), allied with clear SEM images (Fig. S13[†]), suggests the resilience of the molecular catalyst at this low pH medium. Therefore, the inflection observed in Fig. 6 might be associated with concerted activity between formation of a copper hydride species and a facilitated delivery of a proton, likely bound to the uncoordinated pyridine arm of the ligand, as described in structure **D** of Fig. 5. This assisted delivery of a proton *via* ligand protonation has been observed in [FeFe] hydrogenases,^{35–37} linked to the high TOFs observed in the Ni^{II}-containing Dubois catalyst,³⁸ and is commonly referred to as a relay mechanism.³⁹ Furthermore, Siegbahn *et al.*³⁵ have suggested an analogous mechanism for the Cu(bztpen) catalyst¹⁸ *via* DFT methods. Here we investigate the possibility of such relay mechanisms using a similar methodology.

Assessment of relay mechanisms

We have demonstrated experimentally that in MeCN the unmetallated ligand can be protonated in presence of 1–3 equiv. of trifluoroacetic acid (Fig. S14a[†]). Although complex protonation has been previously reported,^{40,41} compound **2** remains unaltered under similar protonation conditions, as used for the ligand (Fig. S14b[†]).

However, it is considerably more challenging to reproduce the desired conditions using D₂O at pH 2.5. Therefore, in order to assess generation of a dangling pyridine and its protonation we have relied on DFT calculations to show that the Cu^I complex **2** (described as **A** in Fig. 5) easily generates a species **A'** with a detached pyridine moiety. Further scrutiny shows that dissociation of distinct vicinal pyridine moieties can be considered isoenergetic (Fig. S15[†]). Independent on which pyridine is detached, the resulting species displays a tetrahedral geometry around the Cu^I center.^{42,43} Therefore, several possible pathways that lead to protonation of the dangling pyridine have been considered and are summarized in Fig. S16[†].³⁵ The most likely pathway is shown in Fig. 7. It starts with the five-coordinate Cu^{II} complex **1** being reduced by one electron to yield the Cu^I complex **A'** *via* prior formation of **A**. Protonation

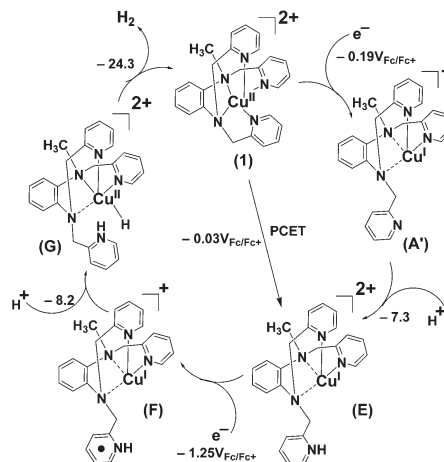


Fig. 7 Catalytic mechanism of H₂ generation by **1** in water at pH 2.5. It involves a proton-coupled electron transfer pathway from **1** to generate the pyridine-protonated Cu^I species **E**. Free energies are in kcal mol⁻¹.

of the nitrogen in the dangling pyridine is possible at pH 2.5 since the p*K*_a of the pyridinium ion is 5.2 in water.⁴⁴ Consequently, at such pH this protonation event is favorable by 7.3 kcal mol⁻¹. The resulting complex **E** can accept one more electron on the pyridinium moiety to give rise to intermediate **F** at a calculated reduction potential of $-1250\text{ mV}_{\text{Fc}/\text{Fc}^+}$. Protonation of **F** on Cu^I leads directly to the Cu^{II}-H⁻ species **G** bypassing the energetically costly Cu^{III}-H⁻ intermediate. The Cu^I center in **F** donates only one electron to the incoming proton and the second electron is donated from the reduced pyridine moiety. This protonation event is favorable by 8.2 kcal mol⁻¹. The hydrogens on the pyridine nitrogen and the Cu^{II} center in **G** are only 1.63 Å apart from each other. The last process requires intramolecular coupling of these two hydrogens in **G** and thus, H₂ is formed and released. This process is favorable by 24.3 kcal mol⁻¹. The resulting complex **1** can accept one electron and reenter the catalytic cycle. PCET step may possible direct conversion of **1** into **E**. The Mulliken spin density plots of different Cu complexes and calculated decomposition pathways of catalyst **1** are shown in Fig. S17 and S18[†]. DFT calculations find that the potentials required for catalytic H₂ generation are $-1610\text{ mV}_{\text{Fc}/\text{Fc}^+}$ (Fig. 5) at pH = 7 and $-1250\text{ mV}_{\text{Fc}/\text{Fc}^+}$ (Fig. 7) at pH = 2.5.

The experimentally measured onset potentials are $-1900\text{ mV}_{\text{Fc}/\text{Fc}^+}$ at pH = 7 and $-1610\text{ mV}_{\text{Fc}/\text{Fc}^+}$ at pH = 2.5. DFT calculations find that there is an anodic shift of the potential of 360 mV_{Fc/Fc+} resulting from changing the pH from 7 to 2.5. This shift matches quite well with the experimentally measured anodic shift of 290 mV_{Fc/Fc+} for changing the pH from 7 to 2.5 (Fig. S19[†]).

Conclusions

We have investigated the new molecular electrocatalyst [Cu^{II}(L^{N2Py3})](PF₆)₂ (**1**) capable of dihydrogen generation *via*

water reduction. This complex is active at pHs 7 and 2.5. Water reduction by **1** at pH 7 yielded a TON_{3h} of 1670 with an onset potential of $-1900 \text{ mV}_{\text{Fc}^+/\text{Fc}}$ while a TON_{3h} of 3900 was measured at pH 2.5 with an onset potential of $-1610 \text{ mV}_{\text{Fc}^+/\text{Fc}}$.

The catalytic activity of **1** is based on a molecular mechanism, in accordance with the absence of nanoparticulate materials on post-catalytic grafoil electrodes. Pyridine moieties in the ligand framework in complex **1** play a crucial role in bypassing the high-energy $\text{Cu}^{\text{III}}\text{-H}^-$ intermediate in the generation of dihydrogen. A $\text{Cu}^{\text{II}}\text{-H}^-$ species has been proposed and a PCET pathway has been invoked for generation of this $\text{Cu}^{\text{II}}\text{-H}^-$ species.

Both the experimental and theoretical studies indicate that different mechanisms are operative at pHs 7 and 2.5. At the lower pH protonation of a dangling pyridine leads to a relay mechanism associated with an increased charge consumption over time. The pyridine moiety gets protonated and dihydrogen generation proceeds *via* intramolecular coupling with the hydride of the $\text{Cu}^{\text{II}}\text{-H}^-$ moiety.

Although we succeeded in obtaining molecular catalysis, the proposed design based on ligand $\text{L}^{\text{N}2\text{Py}3}$ conferred limited robustness. Considering the successful use of this ligand for vigorous cobalt¹⁰ and nickel³⁴ catalysts, one can conclude that the development of copper-based catalysts will require even sturdier frameworks capable of handling (i) the geometrical changes associated with the $\text{Cu}^{\text{II}}/\text{Cu}^{\text{I}}$ redox couple, and (ii) the intrinsic lability of these ions.

Materials, methods and synthetic procedures

General. Reagents and solvents were used as received from commercial sources without further purification. Infrared spectra were recorded from $4000\text{--}650 \text{ cm}^{-1}$ as KBr pellets on a Bruker Tensor 27 FTIR spectrophotometer. ¹H-NMR spectra were obtained in Mercury FT-NMR 400 MHz and Varian VNMRS 500 MHz instruments using CDCl_3 and CD_3CN as solvents. ESI-(+) mass spectrometry was performed in a triple quadrupole Micromass Quattro LC equipment. Elemental analysis for C, H and N was carried out using an Exter CHN analyzer by Midwest Microlab: Indianapolis, Indiana. UV-Visible spectra were obtained with quartz cells at room temperature in a UV-3600 Shimadzu spectrophotometer operating in the range of 190 to 1600 nm. Values of ϵ are given in $\text{mol L}^{-1} \text{ cm}^{-1}$. X-band (9.37 Hz) EPR spectra were obtained from $1 \times 10^{-4} \text{ M}$ samples of **1** and bulk-electrolyzed **2** prepared under N_2 atmosphere using a Bruker EMX spectrometer with an ER041XG resonator.

Electrochemistry and bulk electrolysis. The electrochemical behavior of complex **1** was studied in a BAS 50 W potentiostat/galvanostat. Cyclic voltammograms were obtained at room temperature in MeCN solutions containing 0.1 M of *n*-Bu₄NPF₆ as the supporting electrolyte under an inert atmosphere. The electrochemical cell was comprised of three electrodes: glassy carbon (working electrode), Ag/AgCl (reference electrode), Pt wire (auxiliary electrode). The ferrocene/ferrocenium redox couple Fc/Fc^+ ($E^\circ = 400 \text{ mV vs. NHE}$) was used as

the internal standard.²⁵ Reversibility of the peaks were evaluated by calculating the peak-to-peak potential separations ($\Delta E_p = |E_{p,c} - E_{p,a}|$) and $|i_{pa}/i_{pc}|$ values. The catalytic ability of the complex was evaluated by performing a cyclic voltammogram using 1.0 M aqueous phosphate buffer and a three-electrode cell setup: mercury pool (working electrode), Ag/AgCl (reference electrode), and Pt coil (32 cm, auxiliary electrode). Bulk electrolysis experiments were performed in a custom made H-type cell with two compartments separated by a frit. On the first compartment the working electrode and reference electrodes are placed, while the auxiliary electrode is placed on the adjacent compartment. Bulk electrolysis (BE) of the complex was performed in MeCN (20 mL) using TBAPF₆ (tetrabutylammonium hexafluoro phosphate) as the supporting electrolyte under an inert atmosphere until the calculated charge is reached. Before and after UV-Visible spectra were collected on a UV-3600 Shimadzu spectrophotometer.

X-Ray structural determination. A blue plate-shaped crystal ($0.01 \times 0.23 \times 0.42 \text{ mm}$) of **1** was obtained *via* slow evaporation from *i*-PrOH:MeCN (1:1) and mounted on a mitogen loop using paratone oil, whilst the monovalent **2** was recrystallized in a 1:1 mixture of diethyl ether:MeCN yielding orange colored crystals by slow evaporation in the glove box. Diffraction data were collected for both **1** and **2** on a Bruker APEX-II Kappa geometry diffractometer with Mo radiation and a graphite monochromator using a Bruker CCD (charge coupled device) based diffractometer equipped with an Oxford Cryostream low-temperature apparatus. The data were collected at a temperature of 100 K with omega and phi scans of 0.5° per frame for 30 s. The structure for **1** was solved to a resolution of 0.82 \AA with a completeness of 99.7%, whilst **2** was solved to a resolution of 0.82 \AA with a completeness of 99.2%. Both structures were solved by Direct Methods using the SHELXS-97 program which is part of APEX II⁴⁵ and refined by least squares minimizations on F^2 , SHELXL-97,⁴⁶ which is incorporated in OLEX2.⁴⁷ The structure of **1** was solved in the space group $P2_1/C$, whilst **2** was solved in space group $P\bar{1}$. The asymmetric unit of **1** consists of one cationic molecule in the asymmetric unit, and two hexafluorophosphate counterions. The asymmetric unit of **2** consisted of two independent but very similar cationic molecules with one hexafluorophosphate anionic molecule per cationic molecule. Hydrogen atoms were placed in calculated positions for both structures.

Computational methods. Electronic structure calculations were carried out using the B3LYP density functional^{33,34} as implemented in the Gaussian 09 software package.⁴⁸ The SDD basis set and effective core potential⁴⁹ were used for the Cu atom and the 6-31G(d,p) basis set^{50,51} was used for the other atoms. Solvation effects in water were incorporated using the implicit SMD solvation model⁵² and were included during structure optimization. All of the optimized structures were confirmed as minima by harmonic vibrational frequency calculations and the converged wave functions were tested for the SCF stability. The zero-point energy (ZPE), thermal corrections, and entropic contribution were included for the calculation of the free energies. The standard states of 1 M concentration

were considered for all the reactants and products for calculating the free energies of reactions. The literature value of $-270.3 \text{ kcal mol}^{-1}$ was used for the free energy of proton in water.⁵³ The spin density plots (isovalue = 0.004 au) of the complexes were visualized using GaussView.⁵⁴ Changing a standard state from pH 0 to 7 would increase the free energies of the addition of a proton by approximately $9.5 \text{ kcal mol}^{-1}$ and this correction was taken into account for calculation of the reaction energies of the protonation/deprotonation events at pH 7. Similarly, changing from a standard state from pH 0 to 2.5 would increase the free energies of the addition of a proton by approximately $3.4 \text{ kcal mol}^{-1}$ and this correction was taken into account for calculation of the reaction energies of the protonation/deprotonation events at pH 2.5.

The calculation of the reduction potentials (E , in volts, here expressed as mV for consistency) included ZPE, thermal correction, and entropic contribution. The standard thermodynamic equation $\Delta G = -nFE$ was used.

For the proton-coupled electron transfer (PCET) process^{35,55} from complex **A** to complex **D**, the redox potential was calculated using the equation, $E(\mathbf{A}/\mathbf{D}) = E^\circ(\mathbf{A}/\mathbf{C}) + RT \ln(10) \times (\text{p}K_a - \text{pH})$, where $\text{p}K_a$ for complex **D** in water has been calculated to be 16.2 from the free energy change ΔG of the dissociation reaction, $\mathbf{D} \rightarrow \mathbf{C} + \text{H}^+$. The thermodynamic equation used was $\Delta G = 1.364 \times (\text{p}K_a)$ and the pH value of the medium was considered to be 7. $E^\circ(\mathbf{A}/\mathbf{C})$ is the standard reduction potential for reduction of complex **A** to **C**.

The redox potential for the PCET process, from complex **1** to complex **E**, was calculated using the equation, $E(\mathbf{1}/\mathbf{E}) = E^\circ(\mathbf{1}/\mathbf{A}') + RT \ln(10) \times (\text{p}K_a - \text{pH})$, where $\text{p}K_a$ for complex **E** in water has been calculated to be 5.3 from the free energy change ΔG of the dissociation reaction, $\mathbf{E} \rightarrow \mathbf{A}' + \text{H}^+$. The pH value of the medium was considered to be 2.5. $E^\circ(\mathbf{1}/\mathbf{A}')$ is the standard reduction potential for reduction of complex **1** to **A'**.

The redox potential for the PCET process, from complex **E** to complex **G**, was calculated using the equation, $E(\mathbf{E}/\mathbf{G}) = E^\circ(\mathbf{E}/\mathbf{F}) + RT \ln(10) \times (\text{p}K_a - \text{pH})$, where $\text{p}K_a$ for complex **G** in water has been calculated to be 6.0 from the free energy change ΔG of the dissociation reaction, $\mathbf{G} \rightarrow \mathbf{F} + \text{H}^+$. The pH value of the medium was considered to be 2.5. $E^\circ(\mathbf{E}/\mathbf{F})$ is the standard reduction potential for reduction of complex **E** to **F**. All the calculated potentials were referenced to a value of $E_{1/2} = 4.01 \text{ V}$ for the ferrocene/ferrocenium couple calculated under our level of theory.

Catalytic activity. Water reduction catalysis was evaluated by performing a CV experiment in 1.0 M phosphate buffer solution, which was prepared by mixing NaH_2PO_4 (0.454 mol, 27.24 g) and Na_2HPO_4 (0.545 mol, 38.695 g) in ultrapure water and titrated to pH 7 by adding NaOH or HCl as needed. pH 2.5 phosphate buffer was prepared using 57.660 g of H_3PO_4 dissolved in water and titrated to pH with NaOH as needed. A standard three electrode setup was used: mercury pool (W), Ag/AgCl (R), Pt wire (A). When compared to the blank, a positive shift of the catalytic peak was observed in the presence of the compound. An approximate overpotential (η) value was calculated using the difference between the potential at which

the peak appears and that of the thermodynamic potential. BE experiments in 1.0 M phosphate buffer (pH 7 & pH 2.5) using a custom-made bicompartamental H-type cell with a separatory frit were carried out to generate hydrogen gas electrocatalytically from the complex. The main chamber was filled with 20 mL phosphate buffer and the glass-fitted chamber was filled with 5 mL phosphate buffer. The electrode setup is identical to the CV experiment.

A different BE experiment was performed in MeCN with $n\text{-Bu}_4\text{NPF}_6$ as the supporting electrolyte using $1 \times 10^{-4} \text{ M}$ concentration of **1** at an applied potential of -300 mV , sufficient to the $\text{Cu}^{\text{II}}/\text{Cu}^{\text{I}}$ process. Hydrogen gas production after 3 h was measured using a Gow-Mac 400 gas chromatograph coupled with a thermal conductivity detector. Known volumes of hydrogen gas were injected into the GC and peak areas were determined. Volumes were converted into moles (n) of hydrogen using an ideal gas equation. A calibration curve was then obtained by plotting moles of hydrogen vs. peak area (see example of calculation in the ESI†). After the BE experiment, the contents of 100 μL of headspace were injected into the GC to determine the total amount of hydrogen gas produced.

Scanning electron microscopy. SEM images of the rinsed grafoil electrode were obtained after BE in 1.0 M phosphate buffer, using a SM 7600FE type instrument with a Schottky field emission gun and fully automatic control. A comparison was also made with the SEM image of the grafoil electrode in the absence of the post-catalysis compound.

Synthetic procedures

$\text{N}_2\text{N}'_3$: The ligand $\text{N}_2\text{N}'_3$ was synthesized and characterized according to reported procedure.¹⁰

$[\text{Cu}^{\text{II}}(\text{L}^{\text{N}_2\text{Py}_3})]^{2+}$ (1**).** The purified ligand was stirred at room temperature with $\text{CuCl}_2 \cdot 2\text{H}_2\text{O}$ in methanol (20 mL) for two hours under aerobic conditions, followed by the addition of ammonium hexafluorophosphate to exchange the counterions in the complex. Blue-colored X-ray quality crystals were obtained by crystallizing the complex from $i\text{-PrOH}:\text{MeCN}$ (1:1) mixture. Yield: 90%. ESI/MS in MeCN: $m/z = 229.1$ for $[\text{Cu}^{\text{II}}(\text{L})]^{2+}$. IR (KBr, cm^{-1}): 3084 (w) (aromatic CH); 2992 (w), 2919 (w), 2839 (w) (aliphatic CH); 1590 (s) (C=N); 1433 (s) (C=C); 940 (s) (PF_6^-). Anal. calc. for $\text{C}_{25}\text{H}_{25}\text{CuF}_{12}\text{N}_5\text{P}_2$: C, 40.09; H, 3.36; N, 9.35. Found: C, 40.04; H, 3.35; N, 9.30.

$[\text{Cu}^{\text{I}}(\text{L}^{\text{N}_2\text{Py}_3})]^+$ (2**).** This complex was synthesized using standard glove box techniques. The ligand was stirred at room temperature with $[\text{Cu}(\text{CH}_3\text{CN})_4]\text{PF}_6$ in dry MeCN for 2 h followed by adding diethyl ether to form a 1:1 mixture for slow evaporation. X-ray quality orange crystals were obtained after a week. $^1\text{H-NMR}$ [500 MHz, CD_3CN , 300 K] $\delta/\text{ppm} = 2.42$ [s, 3H (methyl)]; 4.09 [s, 2H (CH_2)]; 4.32 [s, 4H (CH_2)]; 7.18 [m, 2H (aryl)]; 7.24 [m, 5H (aryl)]; 7.33 [m, 2H (aryl)]; 7.56 [t, 1H (aryl)]; 7.67 [t, 2H (aryl)]; 7.74 [t, 1H (aryl)]; 8.58 [d, 2H (aryl)]; 8.69 [d, 1H (aryl)]. Anal. calc. for $\text{C}_{25}\text{H}_{25}\text{CuF}_6\text{N}_5\text{P}$: C, 49.71; H, 4.17; N, 11.59. Found: C, 50.88; H, 4.54; N, 11.76.

Conflicts of interest

There are no conflicts to declare.

Acknowledgements

This work was partially supported by the U.S. Department of Energy, Office of Science, Office of Basic Energy Sciences under award DE-SC0001907 to CNV and HBS. DMBE also acknowledges the Department of Chemistry at WSU for a Thomas C. Rumble Graduate Fellowship. We thank Prof. Jennifer Stockdill for relevant NMR discussions.

Notes and references

- 1 Y. Sun, J. P. Bigi, N. A. Piro, M. L. Tang, J. R. Long and C. J. Chang, *J. Am. Chem. Soc.*, 2011, **133**, 9212–9215.
- 2 C. C. L. McCrory, C. Uyeda and J. C. Peters, *J. Am. Chem. Soc.*, 2012, **134**, 3164–3170.
- 3 O. R. Luca, S. J. Konezny, J. D. Blakemore, D. M. Colosi, S. Saha, G. W. Brudvig, V. S. Batista and R. H. Crabtree, *New J. Chem.*, 2012, **36**, 1149–1152.
- 4 P. Zhang, M. Wang, Y. Yang, D. Zheng, K. Han and L. Sun, *Chem. Commun.*, 2014, **50**, 14153–14156.
- 5 Y. Na, M. Wang, K. Jin, R. Zhang and L. Sun, *J. Organomet. Chem.*, 2006, **691**, 5045–5051.
- 6 R. Mejia-Rodriguez, D. Chong, J. H. Reibenspies, M. P. Soriaga and M. Y. Darensbourg, *J. Am. Chem. Soc.*, 2004, **126**, 12004–12014.
- 7 W. M. Singh, T. Baine, S. Kudo, S. Tian, X. A. N. Ma, H. Zhou, N. J. DeYonker, T. C. Pham, J. C. Bollinger, D. L. Baker, B. Yan, C. E. Webster and X. Zhao, *Angew. Chem., Int. Ed.*, 2012, **51**, 5941–5944.
- 8 T. Fang, L.-Z. Fu, L.-L. Zhou, S.-Z. Zhan and S. Chen, *Electrochim. Acta*, 2015, **178**, 368–373.
- 9 B. D. Stubbert, J. C. Peters and H. B. Gray, *J. Am. Chem. Soc.*, 2011, **133**, 18070–18073.
- 10 D. Basu, S. Mazumder, X. Shi, H. Baydoun, J. Niklas, O. Poluektov, H. B. Schlegel and C. N. Verani, *Angew. Chem., Int. Ed.*, 2015, **54**, 2105–2110.
- 11 C. T. Lyons and T. D. P. Stack, *Coord. Chem. Rev.*, 2013, **257**, 528–540.
- 12 L. Benisvy, E. Bill, A. J. Blake, D. Collison, E. S. Davies, C. D. Garner, G. McArdle, E. J. L. McInnes, J. McMaster, S. H. K. Ross and C. Wilson, *Dalton Trans.*, 2006, 258–267.
- 13 F. Michel, F. Thomas, S. Hamman, C. Philouze, E. Saint-Aman and J.-L. Pierre, *Eur. J. Inorg. Chem.*, 2006, **2006**, 3684–3696.
- 14 A. Kochem, O. Jarjayes, B. Baptiste, C. Philouze, H. Vezin, K. Tsukidate, F. Tani, M. Orio, Y. Shimazaki and F. Thomas, *Chem. – Eur. J.*, 2012, **18**, 1068–1072.
- 15 M. Kugler, J. Scholz, A. Kronz and I. Siewert, *Dalton Trans.*, 2016, **45**, 6974–6982.
- 16 L.-L. Zhou, T. Fang, J.-P. Cao, Z.-H. Zhu, X.-T. Su and S.-Z. Zhan, *J. Power Sources*, 2015, **273**, 298–304.
- 17 J.-P. Cao, T. Fang, L.-Z. Fu, L.-L. Zhou and S.-Z. Zhan, *Int. J. Hydrogen Energy*, 2014, **39**, 13972–13978.
- 18 P. Zhang, M. Wang, Y. Yang, T. Yao and L. Sun, *Angew. Chem., Int. Ed.*, 2014, **53**, 13803–13807.
- 19 A. W. Addison, T. N. Rao, J. Reedijk, J. van Rijn and G. C. Verschoor, *J. Chem. Soc., Dalton Trans.*, 1984, 1349–1356.
- 20 R. Balamurugan, M. Palaniandavar and M. A. Halcrow, *Polyhedron*, 2006, **25**, 1077–1088.
- 21 G. A. McLachlan, G. D. Fallon, R. L. Martin and L. Spiccia, *Inorg. Chem.*, 1995, **34**, 254–261.
- 22 C. N. Verani, R. Shanmugam, F. R. Xavier, M. M. Allard and K. K. Kpogo, *Dalton Trans.*, 2013, **42**, 15296–15306.
- 23 J. A. Driscoll, M. M. Allard, L. Wu, M. J. Heeg, S. R. P. da Rocha and C. N. Verani, *Chem. – Eur. J.*, 2008, **14**, 9665–9674.
- 24 D. B. Rorabacher, *Chem. Rev.*, 2004, **104**, 651–698.
- 25 R. R. Gagne, C. A. Koval and G. C. Lisensky, *Inorg. Chem.*, 1980, **19**, 2854–2855.
- 26 M. Suzuki, H. Kanatomi, Y. Demura and I. Murase, *Bull. Chem. Soc. Jpn.*, 1984, **57**, 1003–1007.
- 27 G. Christou, S. P. Perlepes, E. Libby, K. Folting, J. C. Huffman, R. J. Webb and D. N. Hendrickson, *Inorg. Chem.*, 1990, **29**, 3657–3666.
- 28 P. J. Benites, R. C. Holmberg, D. S. Rawat, B. J. Kraft, L. J. Klein, D. G. Peters, H. H. Thorp and J. M. Zaleski, *J. Am. Chem. Soc.*, 2003, **125**, 6434–6446.
- 29 A. K. Ichinaga, J. R. Kirchhoff, D. R. McMillin, C. O. Dietrich-Buchecker, P. A. Marnot and J. P. Sauvage, *Inorg. Chem.*, 1987, **26**, 4290–4292.
- 30 J. A. Simon, W. E. Palke and P. C. Ford, *Inorg. Chem.*, 1996, **35**, 6413–6421.
- 31 V. S. Thoi, Y. Sun, J. R. Long and C. J. Chang, *Chem. Soc. Rev.*, 2013, **42**, 2388–2400.
- 32 P. H. A. Kankanamalage, S. Mazumder, V. Tiwari, K. K. Kpogo, H. Bernhard Schlegel and C. N. Verani, *Chem. Commun.*, 2016, **52**, 13357–13360.
- 33 S. H. Vosko, L. Wilk and M. Nusair, *Can. J. Phys.*, 1980, **58**, 1200–1211.
- 34 C. Lee, W. Yang and R. G. Parr, *Phys. Rev. B: Condens. Matter*, 1988, **37**, 785–789.
- 35 R.-Z. Liao, M. Wang, L. Sun and P. E. M. Siegbahn, *Dalton Trans.*, 2015, **44**, 9736–9739.
- 36 W. Lubitz, H. Ogata, O. Rüdiger and E. Reijerse, *Chem. Rev.*, 2014, **114**, 4081–4148.
- 37 A. Adamska, A. Silakov, C. Lambertz, O. Rüdiger, T. Happe, E. Reijerse and W. Lubitz, *Angew. Chem., Int. Ed.*, 2012, **51**, 11458–11462.
- 38 M. L. Helm, M. P. Stewart, R. M. Bullock, M. R. DuBois and D. L. DuBois, *Science*, 2011, **333**, 863–866.
- 39 M. Rakowski DuBois and D. L. DuBois, *Chem. Soc. Rev.*, 2009, **38**, 62–72.
- 40 E. V. Rybak-Akimova, A. Y. Nazarenko and S. S. Silchenko, *Inorg. Chem.*, 1999, **38**, 2974–2980.

- 41 A. M. Herrera, R. J. Staples, S. V. Kryatov, A. Y. Nazarenko and E. V. Rybak-Akimova, *Dalton Trans.*, 2003, 846–856.
- 42 N. M. Villeneuve, R. R. Schroeder, L. A. Ochrymowycz and D. B. Rorabacher, *Inorg. Chem.*, 1997, **36**, 4475–4483.
- 43 S. S. Hindo, R. Shakya, N. S. Rannulu, M. M. Allard, M. J. Heeg, M. T. Rodgers, S. R. P. da Rocha and C. N. Verani, *Inorg. Chem.*, 2008, **47**, 3119–3127.
- 44 R. Linnell, *J. Org. Chem.*, 1960, **25**, 290–290.
- 45 APEX2 V2008.5-0 Software for the CCD Detector System, Bruker Analytical X-ray Systems, Madison, WI, 2008.
- 46 G. Sheldrick, *Acta Crystallogr., Sect. A: Fundam. Crystallogr.*, 2008, **64**, 112–122.
- 47 O. V. Dolomanov, L. J. Bourhis, R. J. Gildea, J. A. K. Howard and H. Puschmann, *J. Appl. Crystallogr.*, 2009, **42**, 339–341.
- 48 M. J. Frisch, G. W. Trucks, H. B. Schlegel, G. E. Scuseria, M. A. Robb, J. R. Cheeseman, G. Scalmani, V. Barone, B. Mennucci, G. A. Petersson, H. Nakatsuji, M. Caricato, X. Li, H. P. Hratchian, A. F. Izmaylov, J. Bloino, G. Zheng, J. L. Sonnenberg, M. Hada, M. Ehara, K. Toyota, R. Fukuda, J. Hasegawa, M. Ishida, T. Nakajima, Y. Honda, O. Kitao, H. Nakai, T. Vreven, J. A. Montgomery Jr., J. E. Peralta, F. Ogliaro, M. Bearpark, J. J. Heyd, E. Brothers, K. N. Kudin, V. N. Staroverov, T. Keith, R. Kobayashi, J. Normand, K. Raghavachari, A. Rendell, J. C. Burant, S. S. Iyengar, J. Tomasi, M. Cossi, N. Rega, J. M. Millam, M. Klene, J. E. Knox, J. B. Cross, V. Bakken, C. Adamo, J. Jaramillo, R. Gomperts, R. E. Stratmann, O. Yazyev, A. J. Austin, R. Cammi, C. Pomelli, J. W. Ochterski, R. L. Martin, K. Morokuma, V. G. Zakrzewski, G. A. Voth, P. Salvador, J. J. Dannenberg, S. Dapprich, A. D. Daniels, O. Farkas, J. B. Foresman, J. V. Ortiz, J. Cioslowski and D. J. Fox, *Gaussian 09, Revision D.01*, Gaussian, Inc., Wallingford, CT, 2013.
- 49 M. Dolg, U. Wedig, H. Stoll and H. Preuss, *J. Chem. Phys.*, 1987, **86**, 866–872.
- 50 P. C. Hariharan and J. A. Pople, *Theor. Chim. Acta*, 1973, **28**, 213–222.
- 51 M. M. Francl, W. J. Pietro, W. J. Hehre, J. S. Binkley, M. S. Gordon, D. J. DeFrees and J. A. Pople, *J. Chem. Phys.*, 1982, **77**, 3654–3665.
- 52 A. V. Marenich, C. J. Cramer and D. G. Truhlar, *J. Phys. Chem. B*, 2009, **113**, 6378–6396.
- 53 C. P. Kelly, C. J. Cramer and D. G. Truhlar, *J. Phys. Chem. B*, 2006, **110**, 16066–16081.
- 54 R. Dennington, T. Keith and J. Millam, *Version 5 ed*, Semichem Inc., Shawnee Mission, KS, 2009.
- 55 J. T. Muckerman and E. Fujita, *Chem. Commun.*, 2011, **47**, 12456–12458.